NANO · MICRO small
www.small-journal.com

Structural/Compositional-Tailoring of Nickel Hexacyanoferrate Electrodes for Highly Efficient Capacitive Deionization

*Yang Bao, Jinxin Hao, Shu Zhang, Dechun Zhu, and Feihu Li**

Prussian blue analogs (PBAs) represent a crucial class of intercalation electrode materials for electrochemical water desalination. It is shown here that structural/compositional tailoring of PBAs, the nickel hexacyanoferrate (NiHCF) electrodes in particular, can efficiently modulate their capacitive deionization (CDI) performance (e.g., desalination capacity, cyclability, selectivity, etc.). Both the desalination capacity and the cyclability of NiHCF electrodes are highly dependent on their structural/compositional features such as crystallinity, morphology, hierarchy, and coatings. It is demonstrated that the CDI cell with hierarchically structured NiHCF nanoframe (NiHCF-NF) electrode exhibits a superior desalination capacity of 121.38 mg g^{-1}, a high charge efficiency of up to 82%, and a large capacity retention of 88% after 40 cycles intercalation/deintercalation. In addition, it is discovered that coating of carbon (C) film over NiHCF can lower its desalination capacity owing to the partial blockage of diffusion openings by the coated C film. Moreover, the hierarchical NiHCF-NF electrode also demonstrates a superior selectivity toward monovalent sodium ions (Na^+) over divalent calcium (Ca^{2+}) and magnesim (Mg^{2+}) ions, allowing it to be a promising platform for preferential capturing Na^+ ions from brines. Overall, the structural/compositional tailoring strategies would offer a viable option for the rational design of other intercalation electrode materials applied in CDI techniques.

1. Introduction

The need for clean water is in ever-growing demand globally due in part to climate change, the increase in human population and their living standard, etc.[1,2] At the same time, the ocean accounts for over 97% of the earth's water resource and can serve as a huge and unlimited reservoir for producing clean water based on high-efficiency desalination techniques.[3,4] Conventional desalination techniques such as multi-stage flash (MSF) distillation and reverse osmosis (RO) separation are already well-established and have achieved great success in commercial applications.[5] Nevertheless, emerging alternative technologies have also been developed in recent decades to continuously improve the technologies and reduce the cost of desalination.[6] In particular, capacitive deionization (CDI) has emerged as a robust, nonpolluting, energy-efficient, and cost-effective alternative to established technology with great potential for solving the energy-water problems simultaneously over the past two decades.[6–10] CDI technology is based on electrosorption occurring at the electrode/water interface by the electric field applied between an electrode pair. Therefore, the adsorption capacity of the electrode plays a crucial role in determining the performance of CDI.

A broad spectrum of electrode materials has been intensively explored so far toward improving their salt adsorption capacities (SACs) and energy efficiency.[11–14] Among these electrode materials, Prussian blue analogs (PBAs) have attracted great attention due in part to their tunable 3D open frameworks or cage-like structures that enable massive insertion and storage of both molecular and ionic species.[15–18] Such intrinsic large spacings inside PBAs, for example, copper hexacyanoferrate (CuHCF) and nickel hexacyanoferrate (NiHCF), along with their long cycle life, excellent energy efficiency, and cost-effectiveness allow them to be a promising candidate for use in energy storage,[15,19,20] and electrochemical desalination.[16,18,21] For instance, using NiHCF electrodes with brackish-water level NaCl/KCl influent, Porada and colleagues demonstrated a SAC of 34 mg g^{-1} in a membrane CDI (MCDI) platform (denoted as the cation intercalation desalination (CID) by the authors).[16] Likewise, Kim et al. showed that CuHCF electrodes can achieve an SAC up to 100 mg g^{-1} in a battery electrode deionization (BDI) system (lately referred to as rocking-chair CDI (RCDI) system) with an influent of 50 mM NaCl and an applied voltage of 0.6 V.[21] In an RCDI platform with sodium

Y. Bao, J. Hao, S. Zhang, F. Li
Collaborative Innovation Center of Atmospheric Environment and Equipment Technology
Jiangsu Key Laboratory of Atmospheric Environment Monitoring and Pollution Control
School of Environmental Science and Engineering
Nanjing University of Information Science and Technology
219 Ningliu Road, Nanjing 210044, China
E-mail: fhli@nuist.edu.cn
D. Zhu, F. Li
NUIST Reading Academy
Nanjing University of Information Science and Technology
219 Ningliu Road, Nanjing 210044, China
The ORCID identification number(s) for the author(s) of this article can be found under https://doi.org/10.1002/smll.202300384.

DOI: 10.1002/smll.202300384

nickel hexacyanoferrate (NaNiHCF) and sodium iron hexacyanoferrate (NaFeHCF) electrodes, Lee et al. reported an SAC of 59.9 mg g^{-1} for an influent of 0.5 M NaCl that was desalted at a constant current (±0.5 mA cm^{-2}) mode.[22]

However, the continuous insertion/extraction of cations in the PBA electrode (e.g., NiHCF) can lead to the collapse of the PBA lattice, which is likely to reduce the desalination capacity as well as the cycling stability. Therefore, it remains important to develop PBA materials with remarkable electrochemical desalination performance, and excellent cycling stability. To improve the desalination capacity and/or stability of such electrodes, integrating them with carbon-based materials such as reduced graphene oxide (rGO),[23] graphene aerogel (GA),[24] 3D carbon nanosheet networks (3DC),[25] carbon cloth,[26,27] and carbon nanotubes (CNTs)[28] is a feasible and promising strategy. A recent report has demonstrated an SAC as high as 107.5 mg g^{-1} for NiHCF@3DC-2//activated carbon electrodes in a hybrid CDI (HCDI) cell with an influent of 20 000 mg L^{-1} and a cell voltage of 1.2 V.[25] Besides, incorporating PBAs with other non-carbon materials such as Nafion,[29] and $Ti_3C_2T_x$ MXene[30] can also improve their stability and/or adsorption capacity toward sodium ions. At the same time, it was found that the desalination performance of PBA electrodes can be efficiently enhanced by compositional optimizing[31] and/or structural tailoring.[26,27,32] A recent study has shown that PBA nanoframes with high crystallinity and a large contactable surface area show remarkable rate performance and cycling stability for sodium/lithium-ion insertion/extraction.[33] Rehman et al. found that high-quality NiHCF (also with high crystallinity) exhibited a high specific capacity and notable cycling stability without noticeable fading in capacity retention after 1200 cycles, which makes such PBA a promising long-life cathode material for sodium-ion batteries.[34] Nevertheless, the capacitive desalination behavior of these PBAs with such hierarchical structure or high crystallinity has yet to be systematically evaluated. In addition, it is reported that coating with carbon or nitrogen can lead to improved conductivity and stability of non-carbon electrode materials such as TiO_2,[35] and $Na_4Ti_9O_{20}$ (NTO).[36] However, the impact of carbon or carbon/nitrogen-coating on the electrochemical property of PBA electrodes and thereby their capacitive desalination performance remains unexplored so far. The effort on tailoring PBA for CDI platform, both structurally and compositionally is far from sufficient, and few studies have yet been conducted to systematically compare the above two tailoring strategies for constructing robust and high-efficiency CDI systems.

Herein, we comprehensively compare the structural tailoring with the compositional tailoring of NiHCF materials toward applications in CDI platform by preparing and evaluating NiHCF materials with individual structural or compositional features for capacitive desalination. The structural tailoring involves in preparing PBA with cube and nanoframe structures by controlled crystallizing and preferential etching, whereas the compositional tailoring focuses in coating of carbon and/or nitrogen onto PBA surface by hydrothermal post-treatment. Insights into the influences of structural or compositional characteristics on the desalination capacity are investigated through microstructural characterization, electrochemical tests, and CDI desalination experiments. The effects of working voltage and feed concentration on the CDI performance, the cyclability, and the selectivity of NiHCF electrodes toward monovalent ions are examined as well. We found that the structural tailoring strategies are more efficient to improve the CDI performance compared to the compositional tailoring. For instance, benefiting from its hierarchical structure and high crystallinity, the desalination capacity of nanoframe structured NiHCF achieved 121.38 mg g^{-1} at 1.2 V in a feedwater of 500 mg L^{-1}, quite higher than those of other PBA counterparts with varying structural and/or compositional features. This structural tailoring strategies is expected to guide the design of other intercalation electrode materials toward high-performance electrochemical desalination.

2. Results and Discussions

2.1. Characterizations of As-Prepared NiHCF Materials

Figure 1a shows the structural/compositional tailoring strategies, by which four tailored NiHCF along with one conventional NiHCF nanoparticle were prepared. As shown in Figure 1b, the XRD patterns of all the as-prepared NiHCF samples exhibit a similar profile that can be classified as cubic F–43m group with a set of reflections well matched with the standard card of JCPDS # 86–0501. Note that the peaks at (220), (420), and (440) reflections of NiHCF, NiHCF-HQ, and NiHCF-NF have split into two equal branches, which is believed to stem from the expansion of the lattice and thereby the decrease in symmetry caused by their intrinsic alkali metal ions.[34] As hydrothermal treatment can often yield crystals with high symmetry,[35,36] it is as expected that coating with C or C/N at elevated temperature (Text S1, Supporting Information) can enhance the symmetry of NiHCF@C and NiHCF@N/C as indicated by the unsplit peaks at the same reflections mentioned above. Interestingly, the peak intensity at the (200) reflections decreases slightly in the order NiHCF@N/C < NiHCF@C < NiHCF < NiHCF-NF < NiHCF-HQ, indicative of the decrease in crystallinity of these materials in the same order.[31] The high crystallinity of NiHCF-HQ is because the precursor, trisodium citrate limits the slow release of nickel ions (Ni^{2+}) during the coprecipitation process, which inhibits the coprecipitation rate with sodium ferrocyanide, thereby resulting in an extremely well-crystallized NiHCF-HQ.[34]

XRF analyses of these NiHCF samples confirm the existence of two major elements, that is, Fe and Ni (Figure 1c). Furthermore, the surface Fe/Ni atomic ratios varied over the range of 1.14–1.86 for these materials (Table S1, Supporting Information), which are higher than that of bulk NiHCF cube as measured by inductively coupled plasma-optical emission spectroscopy (ICP-OES),[33] implying that Fe atoms are likely to expose on the external surfaces and that HCl etching can disassemble the exterior $[Fe(CN)_6]^{3-}$ complexes from the NiHCF framework as observed earlier.[33] Figure 1d shows the FTIR spectra of these as-prepared NiHCF samples. The characteristic infrared bands at 3610, 3410, and 1610 cm^{-1} are assignable to the stretching of hydroxyl groups and the bending of water molecules, respectively.[34,37] The apparent bands at 2166 and 2100 cm^{-1} are fingerprints of divalent

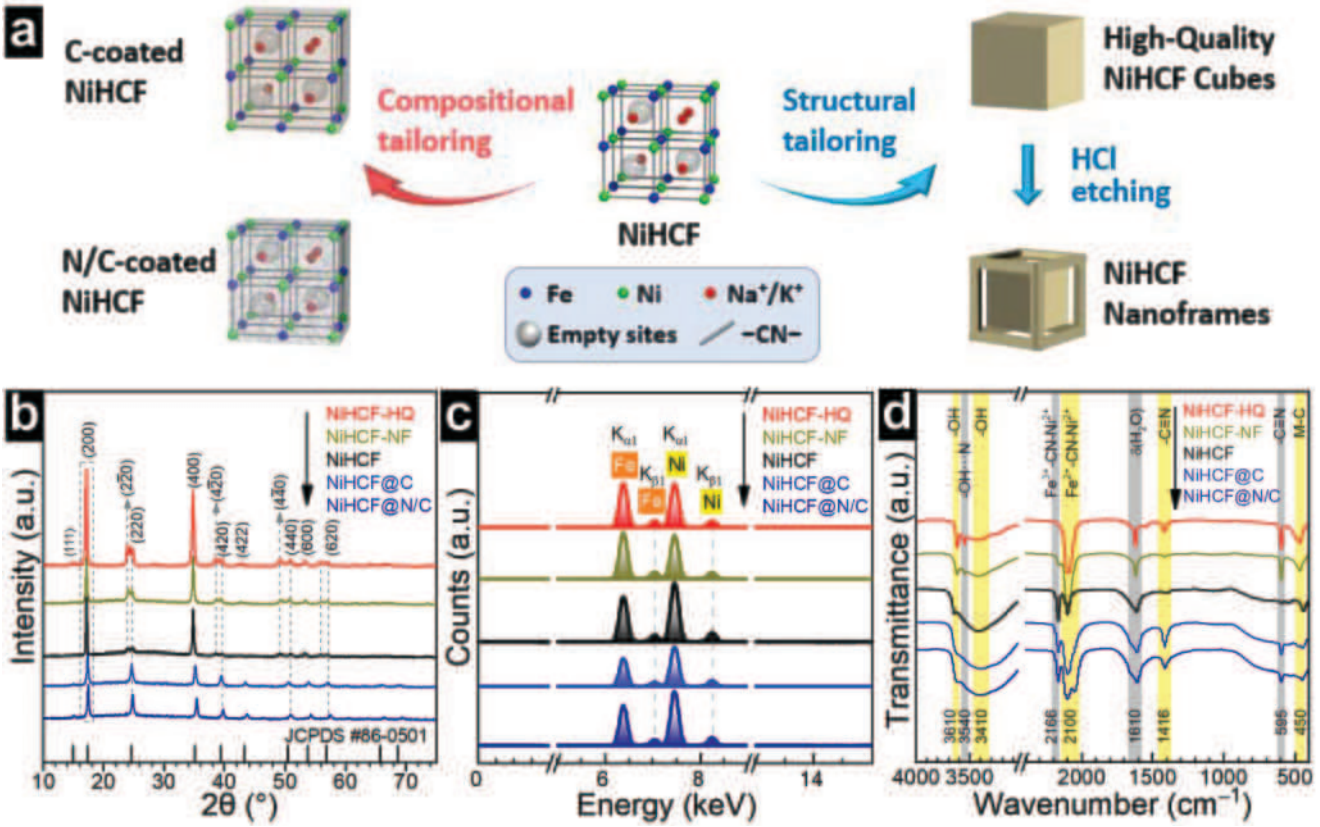

Figure 1. a) Schematic illustration of structural/compositional tailoring of NiHCF. b) XRD patterns. c) XRF spectra. d) FTIR spectra of NiHCF, NiHCF-HQ, NiHCF-NF, NiHCF@C, and NiHCF@N/C.

iron (Fe(II)) and trivalent iron (Fe(III)), respectively, that is, Fe^{III}-CN-Ni^{II} and Fe^{II}-CN-Ni^{II},[38] which also indicates the successful synthesis of NiHCF materials. The bands at 1416 and 595 cm^{-1} are ascribed to cyanogroup (C≡N) stretching, whereas that of ≈450 cm^{-1} is indicative of stretching of the metal–carbon bonding.[39] Note that the stretching vibration of cyanogroup were also detected at ≈2158 cm^{-1} by Raman spectroscopy (Figure S5, Supporting Information), and that the Raman intensity of NiHCF decreased correspondingly after C- or N/C-coating. Two weak peaks assignable to the D- and G-band of the sp^3-type carbon and sp^2 graphite-like structure were observed over the range of 1300–1620 cm^{-1}. Both the D- and G-band shifted a little bit to the lower wavenumber region after co-coating of N and C due to the structural defects and edge plane exposure caused by heterogeneous nitrogen atom doping.[40] These findings demonstrate the decomposition of both C and N precursors at elevated temperature (i.e., ≈200 °C) and successful coating of C or N/C onto the pristine NiHCF via the hydrothermal post-treatment. Further increase in hydrothermal temperature clearly benefits the decomposition of precursors, but might lead to thermal decomposing of the pristine NiHCF. It is believed that NiHCF often inherits interstitial water from the synthesis process, which will decrease its desalination ability and structural stability.[41] Note that the intensity of the apparent band at 1610 cm^{-1} of NiHCF, NiHCF@C, and NiHCF@N/C are much higher compared to those of both NiHCF-HQ and NiHCF-NF materials, implying much less content of interstitial water inside the latter two samples. This is likely to attribute to the addition of a chelator (i.e., trisodium citrate), which can facilitate the formation of high-quality NiHCF crystals with lower content of interstitial water, thereby enabling higher desalination performance of the resulting electrodes.

SEM images of these NiHCF materials showed that NiHCF, NiHCF@C, and NiHCF@N/C are composed of large aggregates of irregular nanoparticles (**Figure 2**a–c), in good consistence with earlier observations.[15] After hydrothermal coating with C or N/C, the morphological features of the resulting NiHCF@C and NiHCF@N/C appear to be no apparent change as compared to the parent NiHCF (see Figure 2a–c), implying high hydrothermal stability of such materials. Interestingly, both NiHCF-HQ and NiHCF-NF are featured by a lot of monodispersed cube-shaped particulates with a size of 200–1000 nm (Figure 2d,e). Benefiting from the chelator (i.e., trisodium citrate) that suppressed the growth rate of NiHCF crystal,[34] NiHCF-HQ has a well-defined cubic structure and high crystallinity (Figures 1b,2d). Note that after etching with 0.4 M HCl, the resulting NiHCF-NF is characterized by concave surfaces of each cube with slightly less size (Figure 2e). This is because the surface $[Fe(CN)_6]^{3-}$ complexes of each cube were partially dissolved by HCl, leaving the skeleton composed of the crystal edges and referred to as the PBA nanoframes.[33]

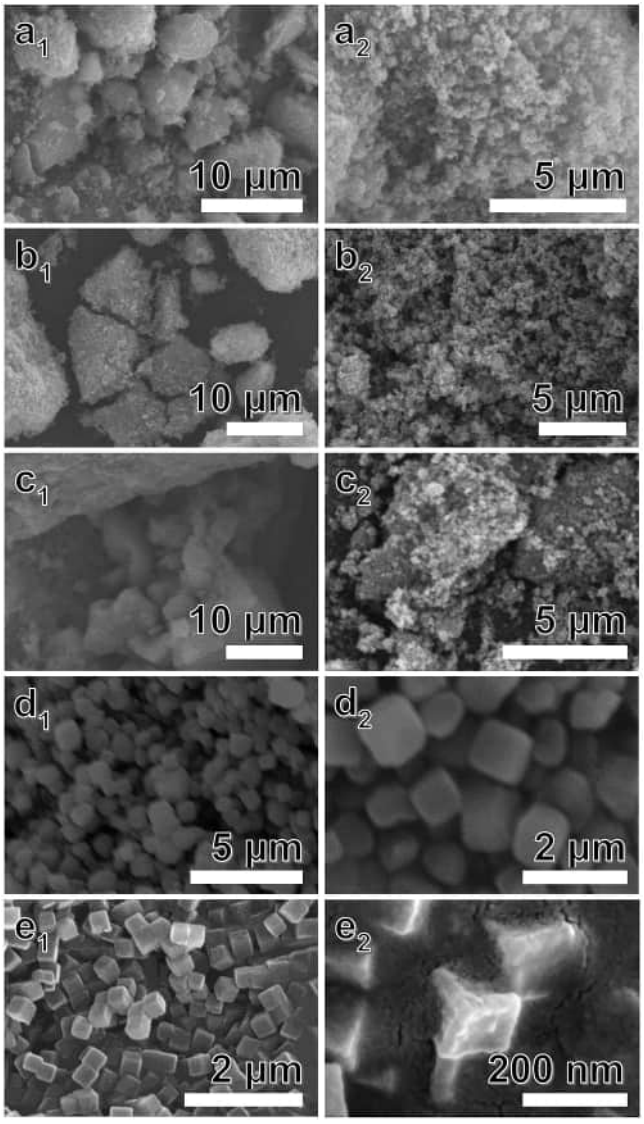

Figure 2. SEM images at different magnifications. a) NiHCF, b) NiHCF@C, c) NiHCF@N/C, d) NiHCF-HQ, and e) NiHCF-NF.

2.2. Electrochemical Properties of NiHCF Electrodes

The electrochemical properties of all NiHCF electrodes are shown in **Figure 3**. CV curves of these electrodes at scanning rates from 5 to 100 mV s^{-1} within a potential window of 0–1.0 V demonstrate a low polarization (Figure S6, Supporting Information). These paired symmetrical peaks over the potential window of 0–1.0 V relate to the redox reaction of the high-spin Fe^{III}/Fe^{II} coordinated with N of cyanogroup (i.e., Fe–N≡C) due to the intercalation/deintercalation of Na^+ ions.[31,38] Note that the CV curves of these electrodes at 5 mV s^{-1} exhibit well-defined redox peaks over the range of 0.4–0.6 V (Figure 3a), indicative of the reversible Faradaic reactions of the NiHCF electrodes (i.e., $ANiFe^{III}(CN)_6 + e^- + A^+ \leftrightarrow A_2NiFe^{II}(CN)_6$, A represents the cation intercalated into the NiHCF crystal structure).[42] Additionally, the NiHCF-NF electrode shows the maximum integrated area under the relevant CV curve, implying the highest ion storage capacity and thereby the superior desalination performance.[37,43] These findings are in good agreement with the GCD results shown in Figure 3b, where the NiHCF-NF electrode exhibits the longest charge/discharge plateau at a specific current of 1 A g^{-1} and voltage from 0.6 to 0.3 V, demonstrating the greatest specific capacity among these electrodes.[32,44] It is noteworthy that all the GCD curves at varying specific currents (Figure S7a–e, Supporting Information) are featured by an obvious charge/discharge plateau with a high degree of symmetry, indicating high reversibility and Faraday behavior of these electrodes.[45] Note that the duration of the charge/discharge plateau is negatively correlated with the specific current, which is because more active sites are filled to transport resistance at a low specific current, thus prolonging the corresponding duration.[45] Moreover, the current resistance (IR) drops measured by the galvanostatic discharge curves exhibit a nearly linear dependence on the specific current and decrease in the order NiHCF-NF < NiHCF-HQ < NiHCF < NiHCF@C < NiHCF@N/C (Figure S7f, Supporting Information). This observation reveals that the NiHCF-NF electrode has the lowest internal charge-transfer resistance (Table S1, Supporting Information) and excellent capacitive performance.[43]

The specific capacitances (F g^{-1}) at different specific currents were calculated from each discharge curve using Equation (S1), Supporting Information, and are depicted in Figure 3c. As the specific currents increase from 0.4 to 2.0 A g^{-1}, the specific capacitances decrease accordingly, and follow the order of NiHCF-NF > NiHCF-HQ > NiHCF > NiHCF@C > NiHCF@N/C. Note that the specific capacitance values at 0.3 A g^{-1} are 435.76, 257.84, 227.77, 132.96, and 101.33 F g^{-1}, for NiHCF-NF, NiHCF-HQ, NiHCF, NiHCF@C, and NiHCF@N/C, respectively (Table S1, Supporting Information). In general, a high specific capacitance implies a high ion storage capacity, which accordingly leads to high desalination capacity when applied in the CDI platform.[4,14] Therefore, it is reasonable to predict that the NiHCF-NF electrode with the highest specific capacitance is likely to demonstrate the best desalination performance among these electrodes. The EIS data were also recorded and analyzed to further elucidate the electrochemical properties of these electrodes (Text S2, Supporting Information). The Nyquist plots shown in Figure 3d show that the NiHCF-NF electrode has the smallest diameter of the semicircle in the high-frequency region (see the inset on the upper-left in Figure 3d), indicative of the least charge-transfer resistance (R_{ct}) value and thus the highest charge transfer rate at the interface between the NiHCF-NF electrode and the electrolyte (i.e., NaCl).[37] Besides, the Warburg impedance values (Z_w) of these electrodes derived from the sloped portions in the intermediate- and low-frequency regions decrease in the order NiHCF@N/C > NiHCF-NF > NiHCF > NiHCF-HQ > NiHCF@C (Figure S8, Supporting Information), indicating that NiHCF@C has the most rapid interfacial ion migration rate, followed by other electrodes in reverse order. Nonetheless, fitting the impedance data with the equivalent circuit inside Figure 3d yields R_{ct} and equivalent series resistance (R_s) of these NiHCF electrodes (Table S1, Supporting Information). On contrary to a previous report,[26] either NiHCF@N/C or NiHCF@C exhibits higher resistances than the pristine NiHCF electrode. A possible explanation for this observation

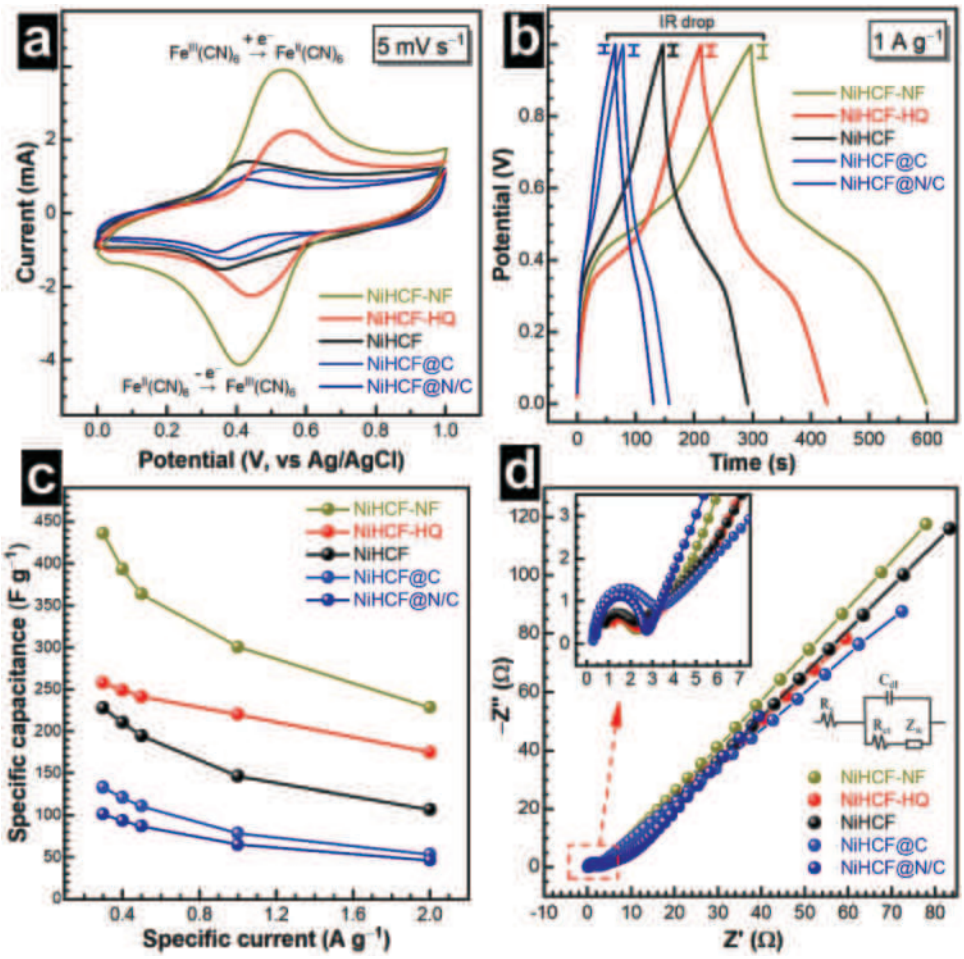

Figure 3. Electrochemical characterizations of all NiHCF electrodes: a) CV curves at 5 mV s^{-1} in 1 M NaCl solution. b) GCD curves at 1 A g^{-1} in 1 M NaCl solution. c) Specific capacitances at different specific currents. d) Nyquist plots of EIS and the fitting curves, inset on the right is the equivalent circuit.

may be that only the outermost layer of precursors (i.e., glucose or PDA) pre-loaded the pristine NiHCF were decomposed and converted into carbon or nitrogen/carbon upon hydrothermal post-treatments. The undecomposed precursor interlayer may block electron or ion transport, thereby affecting the EIS results but not the Raman data. The NiHCF-NF electrode demonstrates the lowest R_{ct} and R_s of 0.97 and 0.42 Ω, respectively (Table S1, Supporting Information). Given the minimum internal charge-transfer resistance of the NiHCF-NF electrode as deduced from the above IR Drop analyses, it is expected that the NiHCF-NF electrode to show the best charge-transfer performance. The unique hierarchical structure and high crystallinity of the NiHCF-NF appear to boost the rapid intercalation and deintercalation of Na^+ ions,[33] thereby allowing for the best electrochemical desalination performance.

2.3. Capacitive Deionization Performance

All desalination experiments were conducted in batch mode and on an RCDI platform (Text S3, Figures S2–S4, Supporting Information). The NiHCF electrodes were initially evaluated at a cell voltage of 1.2 V in a one-sided RCDI cell with 100 mg L^{-1} NaCl (1.71 mM) solution as the feedwater (**Figure 4**). As shown in Figure 4a, the conductivity versus time curves of all NiHCF electrodes exhibit typical two stages—the intercalation stage followed by the deintercalation stage over one charging–discharging cycle (i.e., one desalination-regeneration cycle).[7,9,23] In addition, the NiHCF-NF electrode demonstrates a quite faster and more capture of Na^+ ions over other electrodes in the intercalation stage, confirming the above speculation about the largest desalination capacity of the NiHCF-NF electrode based on the electrochemical analyses. Moreover, quantitative calculations reveal that the NiHCF-NF electrode demonstrates the greatest salt adsorption capacity (SAC) of 97.33 mg g^{-1} at 1.2 V in a 100 mg L^{-1} NaCl solution (Figure 4b), far superior to other electrodes (refer to 77.96 mg g^{-1} for NiHCF-HQ, 61.27 mg g^{-1} for NiHCF, 54.60 mg g^{-1} for NiHCF@C, and 43.33 mg g^{-1} for NiHCF@N/C). Note that these electrodes also show the same trend in the percentage of salt adsorption, with the highest value of 77.2% for NiHCF-NF and the lowest of 36.0% for NiHCF@N/C (Figure 4b). This observation is likely to ascribe to the unique hierarchical structure and the high crystallinity of the NiHCF-NF electrode, allowing for much more amount of sodium ions being intercalated and subsequently stored.[33,37] Specifically, the nanoframe-structured NiHCF with smaller

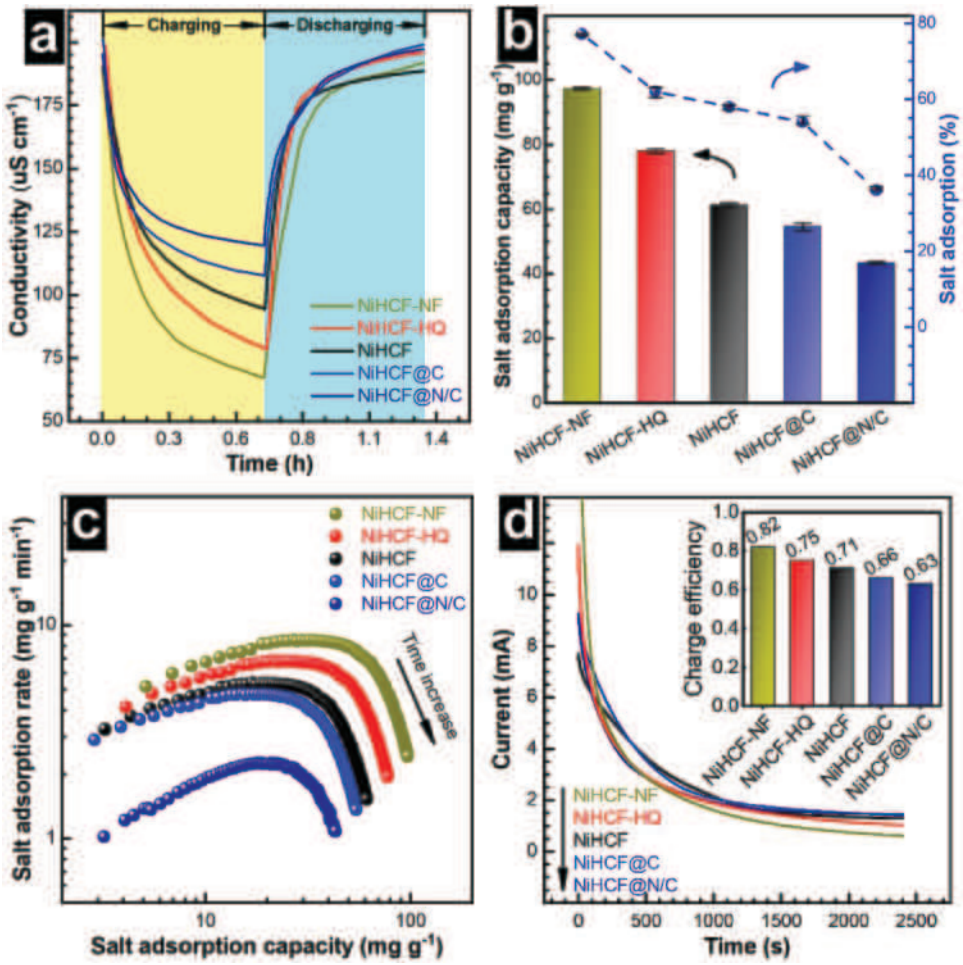

Figure 4. a) Plots of conductivity versus time in the third run of RCDI operation with NiHCF electrodes in 100 mg L^{-1} (1.71 mM) NaCl solution at 1.2 V. b) Salt adsorption capacity and the salt adsorption percentage of all NiHCF electrodes. c) Kim-Yoon plots. d) Current responses and charge efficiency (inset).

particle size and higher surface area than pristine NiHCF cubes, serving as host for intercalated ions, can provide sufficient electrode/electrolyte contact area and reduced diffusion length for electrons and Na^+ ions transfer to realize the higher desalination capacity. In addition, the preferential etching of NiHCF yielded the lowest surface Fe/Ni ratio of 1.14 (Table S1, Supporting Information), indicating the highest concentration of surface defects that can act as additional reaction sites for Na^+ capturing.[33] Interestingly, both the NiHCF@C and NiHCF@N/C electrodes exhibit a smaller desalination capacity even compared to the pristine NiHCF electrode. This phenomenon is likely attributed to the fact that the carbon and nitrogen/carbon films anchored on the original NiHCF surface may hinder the intercalation and/or deintercalation of Na^+ ions,[36] thus diminishing their desalination capacity.

More evidence indicative of the superiority of the NiHCF electrode is depicted in the Kim-Yoon plots (i.e., the salt adsorption rate (SAR) versus SAC profile, Figure 4c), which reveals the fact that the closer the SAR versus SAC profiles are to the upper-right corner of the Kim-Yoon plot, the better the performance of the electrodes in both SAR and SAC.[46] Note that the distance between these SAR versus SAC profiles and the upper-right corner follows the order of NiHCF-NF < NiHCF-HQ < NiHCF < NiHCF@C < NiHCF@N/C (Figure 4c), indicating that the NiHCF-NF electrode can capture Na^+ ions at the fastest rate and in the maximum amount. Figure 4d shows the current response and the charge efficiency of these electrodes in a solution of 100 mg L^{-1} NaCl at 1.2 V. The charging efficiencies are approximately 0.82, 0.75, 0.71, 0.66, and 0.63 for NiHCF-NF, NiHCF-HQ, NiHCF, NiHCF@C, and NiHCF@N/C, respectively. Again, the NiHCF-NF electrode demonstrates the highest charge efficiency under the same circumstances, followed by NiHCF-HQ, NiHCF, NiHCF@C, and NiHCF@N/C. This finding is also in good consistent with the above electrochemical results (Figure 3).

To explore the desalination performance in different scenarios, we also studied the effects of cell voltages and salt concentration in the feedwater on the desalination performance of these electrodes. As shown in **Figure 5**a and Figure S9, Supporting Information, the cell voltages are in direct proportion to either the conductivity of the feedwater or the SACs for all NiHCF electrodes over the voltage range of 0.6–1.2 V. For instance, the SAC of NiHCF-NF electrode drops from 97.33 to 67.90 mg g^{-1} when the cell voltage declines from 1.2 to 0.6 V.

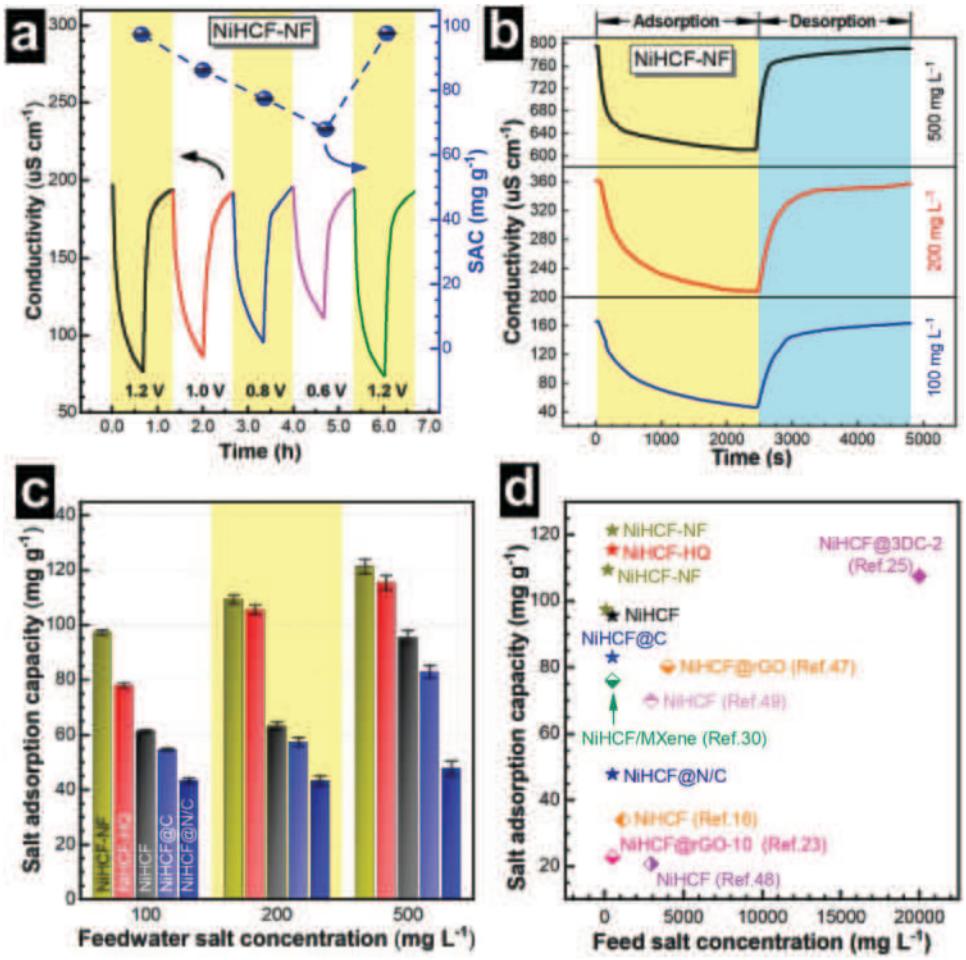

Figure 5. a) Plots of conductivity versus time in CDI cell with the NiHCF-NF electrode in 100 mg L^{-1} NaCl solution at varying cell voltages and plots of SACs versus cell voltage (line with symbols). b) Plots of conductivity versus time in CDI cell with the NiHCF-NF electrode at 1.2 V with varying feed salt concentrations. c) SACs of NiHCF electrodes versus feed salt concentration. d) Comparison in SACs of NiHCF-based electrodes applied for CDI.

However, it is rapidly recovered to as high as 97.74 mg g^{-1} immediately after the cell voltage is being restored to 1.2 V (Figure 5a). Given that a higher cell voltage often yields a greater insertion permittivity for the electrode,[43] a cell voltage of 1.2 V demonstrates the best deionization performance in all cases as earlier observed elsewhere,[14,37] and therefore was adopted as the optimum working voltage to further evaluate the effects of salt concentration (Figure 5b,c; Figure S10, Supporting Information). It is obvious that the higher the salt concentration of the feedwater, the higher the adsorption and desorption rates, and therefore the faster the adsorption and desorption would attain equilibrium (see Figure 5b; Figure S10, Supporting Information). Correspondingly, a larger feedwater salt concentration also leads to a larger SAC (Figure 5c). These findings are in good agreement with previous reports.[43,45] More importantly, the NiHCF-NF electrode demonstrates the greatest SAC as high as 121.38 mg g^{-1} at 1.2 V in a feedwater of 500 mg L^{-1}, followed by NiHCF-HQ (115.42 mg g^{-1}), NiHCF (95.48 mg g^{-1}), NiHCF@C (83 mg g^{-1}), and NiHCF@N/C (47.81 mg g^{-1}). Based on the above results, our NiHCF electrodes, in particular the NiHCF-NF electrode with high-crystallinity and hierarchical structure, are among the best top electrodes compared to other NiHCF electrodes reported in the literature (Figure 5d and **Table 1**),[16,23,26,30,47–49] and also outperform most of the other PBA electrodes (e.g., 100 mg g^{-1} for CuHCF electrode at 0.6 V in a feedwater of 2920 mg L^{-1} NaCl[21]), suggesting that rational structural tailoring of NiHCF is a promising strategy to improve desalination performance and that the highly crystalline NiHCF-NF electrode shows great potential for application in high concentration brine desalination.

2.4. Cycling Performance

To evaluate the long-term cycling performance of these NiHCF electrodes, the cyclability of each electrode were investigated by repeating charge and discharge processes in 500 mg L^{-1} NaCl solution at 1.2 V over 40 runs. The feedwater conductivity and the relevant SAC profiles obtained throughout the cycling tests are presented in **Figure 6**a and Figure S11, Supporting Information. Throughout 40 cycles, the SAC of NiHCF-NF decreased in a nearly linear manner from an initial capacity of 121.38 mg g^{-1} to a final capacity of 106.26 mg g^{c}, corresponding to a capacity retention of 88% (Figure 6a,b). The SAC of NiHCF-HQ, on the

Table 1. Comparison of salt adsorption capacity of PBA electrodes applied for CDI.

Electrodes[a)]	Feedwater salt concentration [mg L^{-1}]	Cell voltage [V]	Cell mode[b)]	Salt adsorption capacity [mg g^{-1}]	Ref.
NiHCF/MXene	500	1.4	HCDI	76	[30]
NiHCF@rGO	4000	1.2	CDI	80.2	[47]
NiHCF	2925	/	BDI	20.7	[48]
NiHCF@3DC-2	20 000	1.2	HCDI	107.5	[25]
NiHCF	2925	/	CDI	70	[49]
NiHCF@rGO-10	500	0.6	HCDI	22.8	[23]
NiHCF	1170	/	CID	34	[16]
CuHCF	2920	0.6	BDI	100	[21]
NiHCF/FeHCF	29 200	0.85	RCDI	59.9	[22]
FeHCF/rGA	2500	1.4[c)]	HCDI	130	[24]
Mn-based PBA	1000	1.0	CDI	10.92	[27]
NiHCF-NF	100	1.2	RCDI	97.33	This study
NiHCF-NF	200	1.2	RCDI	109.37	This study
NiHCF-NF	500	1.2	RCDI	121.38	This study

[a)]MXene, $Ti_3C_2T_x$ dispersion; rGA, reduced graphene aerogel; rGO, reduced graphene oxide; 3DC-2, 3D interconnected carbon nanosheet networks with porous structure; [b)]HCDI, hybrid capacitive deionization; CDI, capacitive deionization; BDI, battery electrode deionization; CID, cation intercalation desalination; RCDI, rocking-chair capacitive deionization; [c)]This was worked under the constant current mode with a current density of 100 mA g^{-1}.

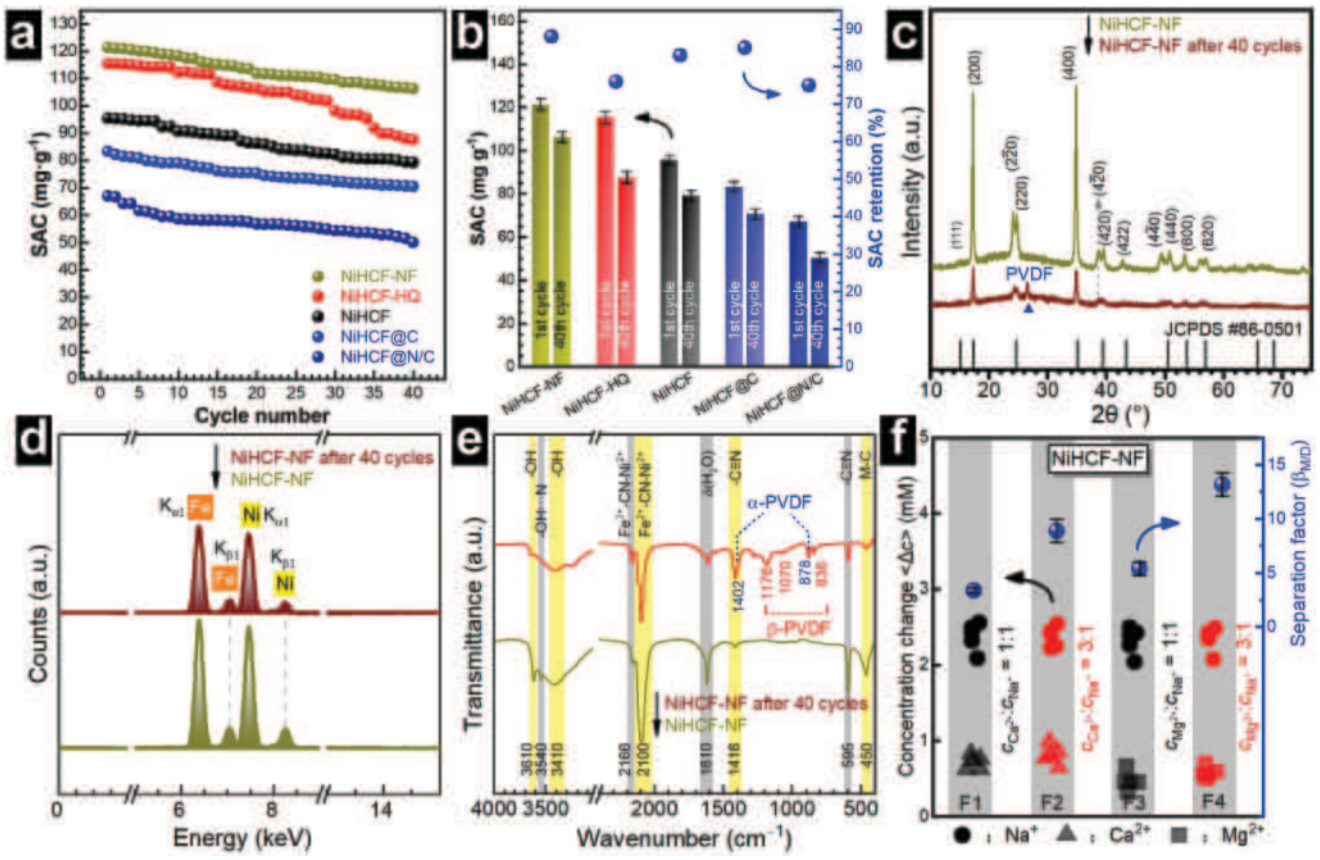

Figure 6. a) Cycling stability of NiHCF electrodes in 500 mg L^{-1} NaCl solution applied in RCDI for 40 charge–discharge runs. b) Comparison in the initial and final SACs of NiHCF electrodes and the corresponding SAC retention rate. c) XRD patterns, d) XRF spectra, and e) FTIR spectra of NiHCF-NF before and after 40-cycles cycling (Note that PVDF indicative in panels (c) and (e) co-existed in the post-cycled NiHCF-NF electrode). f) Selectivity of monovalent Na^+ ions over divalent ions (i.e., Ca^{2+}, Mg^{2+}) of the NiHCF electrode in (F1–F4) feedwaters with varying binary ion mixtures. The separation factor $\beta_{M/D}$, was calculated by dividing the percent of monovalent ions (e.g., Na^+) removed by the percent of divalent ions (e.g., Ca^{2+}) removed simultaneously.

other hand, declined stepwise from 115.42 mg g^{-1} to 87.52 mg g^{-1} over 40 cycles, with a capacity retention of 76% (Figure 6b). Other NiHCF electrodes behaved similarly in the cycling test, in which 83%, 85%, and 75% of the capacity of NiHCF, NiHCF@C, and NiHCF@N/C, respectively, were retained over 40 cycles. Compared to NiHCF-NF, the relatively poor capacity retention of the NiHCF-HQ electrode is most likely ascribed to the hindering of Na^+ ions from diffusing into the central part of the NiHCF-HQ cubes by its high-crystalline and compact surface.[33] The superior cycling performance of the NiHCF-NF electrode over other NiHCF electrodes is believed to be attributed to its high surface-to-volume ratio, and particularly the 3D accessible surface derived from its nanoframe structure, which would offer much more ion accessibility, especially for the central interstitial sites of NiHCF during long-term cycling.[33] Note that the original concave surfaces of each NiHCF-NF particulate have completely disappeared after 40 cycles of intercalation-deintercalation (Figure S11f, Supporting Information), implying the collapse of hierarchical structured nanoframes upon long-term desalination operation. Monitoring the feedwater pH values during the cycling test demonstrates that the intercalation of both Na^+ and hydrogen ions by the NiHCF electrodes can lead to dissociation of water molecules (side reaction), enriching hydroxide ions and thereby increasing the feedwater pH by ≈1.3 unit compared to the initial pH (Figure S12, Supporting Information). Furthermore, PBAs can react with Cl^- and OH^- ions during the cycling tests, and water molecules would occupy the empty sites of PBAs, both of which appear to contribute significantly to the loss of SACs of such electrodes over long-term cycling in NaCl solution.[29,31,34] This can also fully explain why PBA electrodes often show extremely stable cycling over many thousands of cycles with high rate capability in Na^+/Li^+ ion batteries with anhydrous electrolytes.[15,20,41]

As mentioned above, coating with carbon on NiHCF would prevent Na^+ ions from intercalating to some extent,[36] and thereby lowering the SAC of the NiHCF@C electrode compared to the pristine NiHCF. Nonetheless, C-coating seems slightly improve the cyclability of the resulting electrode (Figure 6a,b, SAC retention: 85% for NiHCF@C vs 83% for NiHCF). On the contrary, the N/C co-coated NiHCF@N/C electrode shows the lowest SAC retention, which may be caused by the introduction of Cl^- and NH_4^+ ions from the post-synthesis using glucose and dopamine hydrochloride as coatings. Both ions would react with the PBA,[29,31] and thereby leading to such poor cycling performance.

To further evaluate the structural stability of the NiHCF-NF electrode over 40-cycles cycling, XRD, XRF, and FTIR data of the post-cycled electrode were collected and compared with those of the pristine NiHCF-NF (Figure 6c–e). The crystal structure of NiHCF-NF is quite stable after long-term cycling as indicated by Figure 6c, which shows no phase changes occurred after the 40-cycles cycling test. Likewise, XRF and FTIR spectra also demonstrate no changes in the surface compositions and functional groups upon long-term cycling of the NiHCF-NF electrode (Figure 6d,e). Further experimental evidence from ICP-OES measurements of the cell solution (data not shown) indicates that the loss of Fe and Ni elements from the NiHCF-NF cathode to the bulk solution is less than 3.4% after 40 cycles. The above results indicate that the NiHCF-NF electrode is sufficiently stable and rigid throughout continuous 40-cycles cycling, therefore demonstrating the promise for practical seawater desalination.

2.5. Selectivity

As PBA electrodes often exhibit high ion selectivity when applied to CDI,[16,18,50,51] the mono/divalent ion selectivity of these NiHCF electrodes was also comprehensively explored at 1.2 V in feedwaters with varying binary ions (i.e., F1: Ca^{2+}/Na^+ = 10:10 mM; F2: Ca^{2+}/Na^+ = 30:10 mM; F3: Mg^{2+}/Na^+ = 10:10 mM; F4: Mg^{2+}/Na^+ = 30:10 mM), following the procedure in our previous work.[37] The selectivity, or preference of monovalent ions (e.g., Na^+) over divalent ions (e.g., Ca^{2+}) is quantified by a separation factor, $\beta_{M/D}$ (defined as the ratio of the percent of monovalent ions removed to the percent of divalent ions removed simultaneously).[18] As shown in Figure 6f, the change in concentration (i.e., Δc) of Na^+ ions varied in the range of 2.3–2.6 mM, regardless of its initial relative concentration with the divalent ions (i.e., the Na^+/D^{2+} ratio, D^{2+} = Ca^{2+}, Mg^{2+}), whereas the corresponding Δc of Ca^{2+} and Mg^{2+} oscillated over the range of 0.6–0.9 mM, and 0.4–0.6 mM, respectively, yielding an average separation factor (β) of 3.34, 8.87, 5.38, and 13.13 for feedwaters F1, F2, F3, and F4, respectively. These β values demonstrate the strong preference of the NiHCF-NF electrode toward monovalent Na^+ ions over divalent Ca^{2+} and Mg^{2+} ions, in good agreement with previous reports.[18,52] This trend is also true for other NiHCF electrodes that demonstrate separation factors ranging from 2 to 8 toward Na^+ over divalent ions (Figure S13, Supporting Information). One probable mechanism for this selectivity is that monovalent Na^+ ions are thermodynamically more favorable for intercalation into NiHCF unit cells than divalent ions including Ca^{2+} and Mg^{2+}.[53] Specifically, the absorption energy for Na^+ intercalated in the interstitial sites of NiHCF is lower than that for Ca^{2+}, implying stronger interaction between Na^+ and NiHCF, and therefore the preference of NiHCF toward Na^+ over Ca^{2+}.[53]

In addition, note that the average $\beta_{Na/Mg}$ values are greater than the $\beta_{Na/Ca}$ for feedwaters with the same Na^+/D^{2+} ratio (e.g., F1 vs F3, F2 vs F4), implying a greater preference for Na^+ over Mg^{2+} on these NiHCF electrodes as compared to that of Na^+ over Ca^{2+} (Figure 6f; Figure S13, Supporting Information). This is likely ascribed to the higher dehydration of Mg^{2+} ions compared to Ca^{2+} ions,[53] making it more difficult to intercalate Mg^{2+} into NiHCF unit cells than Ca^{2+} ions. As for individual feedwater, for instance, F1, the average β values decrease clearly in the order NiHCF-NF > NiHCF-HQ > NiHCF > NiHCF@C > NiHCF@N/C, in the same order as their desalination performance discussed above (Figures 4b,5c). This is probably attributed to the unique structural characteristics and thereby electrochemical features of these electrodes. For instance, the nanoframe-like NiHCF-NF with hierarchical structure would certainly provide more and larger ion diffusion channels than NiHCF@N/C coated with N/C films, thus showing greater ion selectivity for the same feedwater. Furthermore, the selectivity for Na^+ over divalent Ca^{2+} and Mg^{2+} ions of the NiHCF-NF electrode is in the range of 3.35–13.13, which is comparable to other intercalation electrodes reported previously.[18,54] Based on the

above analyses, it is evident that our CDI platform with NiHCF-NF electrode demonstrates a high promise for preferential removal of Na^+ ions from saline with high levels of sodium and calcium ions, which is quite promising for practical application in the treatment of effluents from saline calcium coproduction industries.[55]

3. Conclusions

In summary, we demonstrate experimentally that structural/compositional tailoring of NiHCF can significantly alter its desalination performance via an RCDI platform. Specifically, post-synthetic coating of carbon on NiHCF can efficiently improve the long-term cycling stability of the NiHCF@C electrode, but lower its salt adsorption capacity due to the partial blockage of the ion-transport openings in such PBA frameworks by the carbon film. However, post-synthetic coating of carbon and nitrogen on NiHCF would adversely influence both the desalination capacity and the cycling stability of the resultant electrode (i.e., NiHCF@N/C) due to the side-reaction between pristine NiHCF and the nitrogen precursors in the post-synthesis. Interestingly, highly crystalline NiHCF cubes (i.e., NiHCF-HQ) obtained by a chelator-assisted coprecipitation shows an enhanced desalination capacity but poorer cycling stability as compared to conventional NiHCF nanocrystals. More importantly, hierarchical NiHCF nanoframe (i.e., NiHCF-NF) obtained by preferential HCl-etching of highly crystalline NiHCF cubes demonstrates the highest capacity as well as the superior cycling stability among these electrodes studied. In addition, the preliminary results of selectivity tests suggest a high preference for Na^+ over Ca^{2+} and Mg^{2+} ions on these NiHCF electrodes, in good consistence with other PBA electrodes observed previously. Overall, the hierarchically structured and high-crystalline NiHCF-NF demonstrates great potential for seawater desalination, particularly for the preferential removal of Na^+ ions from specific industrial brines. Furthermore, the tailoring strategies in this work are believed to apply to other intercalation electrode materials for electrochemical water desalination.

4. Experimental Section

All chemicals used were of reagent grade quality at least and purchased from Sinopharm Chemical Reagent Co., Ltd. (Shanghai, China) unless otherwise specified. All solutions were prepared using deionized water (DI H_2O,) with resistivity ≥ 18 MΩ cm at 25 °C.

Preparation and Characterization of NiHCF Materials: The synthetic schemes of NiHCF are illustrated in Figure S1, Supporting Information, respectively. Specifically, the NiHCF nanocrystals were synthesized via a coprecipitation technique reported previously.[15] Using glucose and dopamine hydrochloride as coatings, the carbon-coated and nitrogen/carbon-coated NiHCF nanoparticles were prepared via a hydrothermally post-synthesized method,[36] and denoted as NiHCF@C and NiHCF@N/C, respectively. High-quality NiHCF cubes (NiHCF-HQ) were prepared following a chelator-assisted coprecipitation technique,[34] and were further employed as the parent materials for the synthesis of NiHCF nanoframes (NiHCF-NF) via a preferential HCl-etching method.[33] The detailed preparing and tailoring procedures of all NiHCF materials can be found in the Supporting Information (Text S1, Supporting Information).

The crystallographic characteristics of the as-prepared NiHCF materials were analyzed using an XRD-6100 diffractometer (Shimadzu, Japan) at a tube voltage of 40 kV and a tube current of 30 mA with Cu-Kα radiation. X-ray fluorescence spectroscopy (XRF) analysis was conducted on a DELTA DC 4000 analyzer (Olympus, USA) with the soil mode. Fourier transform infrared (FTIR) spectrum measurement was performed using the KBr method on an infrared spectrometer (Nicolet iS5, Thermo Fisher, USA). The morphology of NiHCF samples was examined by scanning electron microscope (SEM) using an SU1510 microscope (Hitachi, Japan) at an accelerating voltage of 1.5 kV.

Electrochemical Measurements: Cyclic voltammetry (CV), galvanostatic charge-discharge (GCD), and electrochemical impedance spectroscopy (EIS) analyses were carried out in 1.0 M NaCl solution with a three-electrode system using a CS310H electrochemical workstation (Correst Instruments Inc., Wuhan, China).[37] The three-electrode configuration is composed of a working electrode, a platinum foil electrode (counter electrode), and an Ag/AgCl (3 M KCl) electrode (reference electrode). The working electrodes were fabricated by combining NiHCF, acetylene black (Alfa Aesar, Shanghai, China), and polyvinylidene fluoride (PVDF, Aladdin Chemical Co.) in an 8:1:1 ratio. The mixture was ground by hand and dispersed in a slurry of 1-methyl-2-pyrrolidinone, which then was deposited onto a graphite paper with a size of 1 cm × 1 cm and dried in a vacuum at 80 °C. More details on electrochemical characterizations are presented in Text S2, Supporting Information.

Capacitive Deionization Experiments: The NiHCF electrodes with a size of 5 cm × 5 cm were prepared following the same method as above for preparing the working electrodes (Text S3, Supporting Information). The desalination experiment was performed in a custom-built RCDI cell with a symmetric configuration (Figures S2,S3, Supporting Information). The RCDI cell and other apparatus were integrated to construct the desalination platform (Figure S4, Supporting Information), which was operated in batch mode and under constant voltage conditions for all the desalination tests. A total of 30 mL saline water was circulated between the RCDI cell with a volume of ≈2.5 mL and the saline reservoir at a flow rate of 40 mL min^{-1}. The conductivity of effluent was consecutively monitored by a DDSJ-308A conductivity meter (INESA Scientific Instrument Co., Shanghai, China) and was used to calculate the salt concentration. The effects of feedwater salt concentration and cell voltage on desalination performance were investigated over the range of 100–50 mg L^{-1} at a voltage ranging from 0.6–1.2 V. More details about the desalination operation are given in Text S3, Supporting Information.

Supporting Information

Supporting Information is available from the Wiley Online Library or from the author.

Acknowledgements

The work was partially supported by the Innovation Training Programme for Undergraduate Students of NUIST (XJDC202210300262). The authors would like to thank Dr. Fengying Li and Mr. Haozhi Liu for their experimental assistance.

Conflict of Interest

The authors declare no conflict of interest.

Data Availability Statement

The data that support the findings of this study are available from the corresponding author upon reasonable request.

Keywords

electrochemical water desalination, electrosorption, Faradaic electrodes, Prussian blue analog, selectivity

Received: January 13, 2023
Revised: April 18, 2023
Published online: April 28, 2023

[1] C. J. Vorosmarty, P. Green, J. Salisbury, R. B. Lammers, *Science* **2000**, *289*, 284.
[2] K. Kummerer, D. D. Dionysiou, O. Olsson, D. Fatta-Kassinos, *Science* **2018**, *361*, 222.
[3] M. Elimelech, W. A. Phillip, *Science* **2011**, *333*, 712.
[4] J. R. Werber, C. O. Osuji, M. Elimelech, *Nat. Rev. Mater.* **2016**, *1*, 16.
[5] A. D. Khawaji, I. K. Kutubkhanah, J. M. Wie, *Desalination* **2008**, *221*, 47.
[6] A. Subramani, J. G. Jacangelo, *Water Res.* **2015**, *75*, 164.
[7] Y. Oren, *Desalination* **2008**, *228*, 10.
[8] M. A. Anderson, A. L. Cudero, J. Palma, *Electrochim. Acta* **2010**, *55*, 3845.
[9] S. Porada, R. Zhao, A. van der Wal, V. Presser, P. M. Biesheuvel, *Prog. Mater. Sci.* **2013**, *58*, 1388.
[10] M. E. Suss, S. Porada, X. Sun, P. M. Biesheuvel, J. Yoon, V. Presser, *Energy Environ. Sci.* **2015**, *8*, 2296.
[11] K. B. Hatzell, M. Boota, Y. Gogotsi, *Chem. Soc. Rev.* **2015**, *44*, 8664.
[12] M. E. Suss, V. Presser, *Joule* **2018**, *2*, 10.
[13] P. Srimuk, X. Su, J. Yoon, D. Aurbach, V. Presser, *Nat. Rev. Mater.* **2020**, *5*, 517.
[14] M. A. Alkhadra, X. Su, M. E. Suss, H. H. Tian, E. N. Guyes, A. N. Shocron, K. M. Conforti, J. P. De Souza, N. Kim, M. Tedesco, K. Khoiruddin, I. G. Wenten, J. G. Santiago, T. A. Hatton, M. Z. Bazant, *Chem. Rev.* **2022**, *122*, 13547.
[15] C. D. Wessells, S. V. Peddada, R. A. Huggins, Y. Cui, *Nano Lett.* **2011**, *11*, 5421.
[16] S. Porada, A. Shrivastava, P. Bukowska, P. M. Biesheuvel, K. C. Smith, *Electrochim. Acta* **2017**, *255*, 369.
[17] Q. Li, Y. Zheng, D. J. Xiao, T. Or, R. Gao, Z. Q. Li, M. Feng, L. L. Shui, G. F. Zhou, X. Wang, Z. W. Chen, *Adv. Sci.* **2020**, *7*, 2002213.
[18] K. Singh, Z. X. Qian, P. M. Biesheuvel, H. Zuilhof, S. Porada, L. C. P. M. de Smet, *Desalination* **2020**, *481*, 114346.
[19] C. D. Wessells, M. T. McDowell, S. V. Peddada, M. Pasta, R. A. Huggins, Y. Cui, *ACS Nano* **2012**, *6*, 1688.
[20] Y. X. Xu, S. S. Zheng, H. F. Tang, X. T. Guo, H. G. Xue, H. Pang, *Energy Storage Mater.* **2017**, *9*, 11.
[21] T. Kim, C. A. Gorski, B. E. Logan, *Environ. Sci. Technol. Lett.* **2017**, *4*, 444.
[22] J. Lee, S. Kim, J. Yoon, *ACS Omega* **2017**, *2*, 1653.
[23] Z. B. Ding, X. T. Xu, Y. Q. Li, K. Wang, T. Lu, L. K. Pan, *Desalination* **2019**, *468*, 114078.
[24] S. Vafakhah, L. Guo, D. Sriramulu, S. Z. Huang, M. Saeedikhani, H. Y. Yang, *ACS Appl. Mater. Interfaces* **2019**, *11*, 5989.
[25] S. Y. Wang, G. Wang, Y. W. Wang, H. R. Song, S. H. Lv, T. Z. Li, C. P. Li, *ACS Appl. Mater. Interfaces* **2020**, *12*, 44049.
[26] X. Y. Zhang, J. Dutta, *ACS Appl. Energy Mater.* **2021**, *4*, 8275.
[27] X. Y. Zhang, E. A. Toledo-Carrillo, D. K. Yu, J. Dutta, *ACS Appl. Mater. Interfaces* **2022**, *14*, 40371.
[28] A. O. Gong, Y. B. Zhao, B. L. Liang, K. X. Li, *J. Colloid Interface Sci.* **2022**, *605*, 432.
[29] J. Ahn, S. Kim, S. I. Jeon, C. Lee, J. Lee, J. Yoon, *Desalination* **2021**, *500*, 114778.
[30] S. Y. Wang, Z. L. Li, G. Wang, Y. W. Wang, Z. Ling, C. P. Li, *ACS Nano* **2022**, *16*, 1239.
[31] M. A. Lumley, D. H. Nam, K. S. Choi, *ACS Appl. Mater. Interfaces* **2020**, *12*, 36014.
[32] Y. B. Zhao, B. L. Liang, X. J. Wei, K. X. Li, C. C. Lv, Y. Zhao, *J. Mater. Chem. A* **2019**, *7*, 10464.
[33] W. Zhang, Y. Y. Zhao, V. Malgras, Q. M. Ji, D. M. Jiang, R. J. Qi, K. Ariga, Y. Yamauchi, J. Liu, J. S. Jiang, M. Hu, *Angew. Chem., Int. Ed.* **2016**, *55*, 8228.
[34] R. Rehman, J. Peng, H. C. Yi, Y. Shen, J. W. Yin, C. Li, C. Fang, Q. Li, J. T. Han, *RSC Adv.* **2020**, *10*, 27033.
[35] S. B. Wang, B. Y. Guan, L. Yu, X. W. Lou, *Adv. Mater.* **2017**, *29*, 1702724.
[36] Z. S. Yue, T. Gao, H. B. Li, *Desalination* **2019**, *449*, 69.
[37] Y. Bao, J. Jin, M. Y. Ma, M. Li, F. H. Li, *ACS Appl. Mater. Interfaces* **2022**, *14*, 46646.
[38] Q. Yang, F. N. Mo, Z. X. Liu, L. T. Ma, X. L. Li, D. L. Fang, S. M. Chen, S. J. Zhang, C. Y. Zhi, *Adv. Mater.* **2019**, *31*, 1901521.
[39] E. Jin, X. F. Lu, L. L. Cui, D. M. Chao, C. Wang, *Electrochim. Acta* **2010**, *55*, 7230.
[40] A. Zahoor, M. Christy, Y. J. Hwang, Y. R. Lim, P. Kim, K. S. Nahm, *Appl. Catal., B* **2014**, *147*, 633.
[41] W. J. Li, C. Han, G. Cheng, S. L. Chou, H. K. Liu, S. X. Dou, *Small* **2019**, *15*, 1900470.
[42] K. J. Tan, X. Su, T. A. Hatton, *Adv. Funct. Mater.* **2020**, *30*, 1910363.
[43] J. Jin, M. Li, M. T. Tang, Y. Li, Y. Y. Liu, H. Cao, F. H. Li, *ACS Sustainable Chem. Eng.* **2020**, *8*, 11424.
[44] W. H. Shi, X. Y. Liu, T. Q. Deng, S. Z. Huang, M. Ding, X. H. Miao, C. Z. Zhu, Y. H. Zhu, W. X. Liu, F. F. Wu, C. J. Gao, S. W. Yang, H. Y. Yang, J. N. Shen, X. H. Cao, *Adv. Mater.* **2020**, *32*, 1907404.
[45] A. Gong, Y. B. Zhao, M. M. He, B. L. Liang, K. X. Li, *Desalination* **2021**, *505*, 114997.
[46] T. Kim, J. Yoon, *RSC Adv.* **2015**, *5*, 1456.
[47] D. V. Cuong, C. H. Hou, *Sep. Purif. Technol.* **2022**, *295*, 121351.
[48] L. Shi, E. Newcomer, M. Son, V. Pothanamkandathil, C. A. Gorski, A. Galal, B. E. Logan, *Environ. Sci. Technol.* **2021**, *55*, 5412.
[49] K. Singh, L. Zhang, H. Zuilhof, L. C. P. M. de Smet, *Desalination* **2020**, *496*, 114647.
[50] W. Shi, P. F. Nie, G. D. Zhu, B. Hu, J. M. Yang, J. Y. Liu, *Chem. Eng. J.* **2020**, *388*, 124162.
[51] Y. S. Xu, H. J. Zhou, G. Z. Wang, Y. X. Zhang, H. M. Zhang, H. J. Zhao, *ACS Appl. Mater. Interfaces* **2020**, *12*, 41437.
[52] T. H. Chen, D. V. Cuong, Y. J. Jang, N. Z. Khu, E. Chung, C. H. Hou, *Chemosphere* **2022**, *307*, 135613.
[53] K. Singh, G. Li, J. Lee, H. Zuilhof, B. L. Mehdi, R. L. Zornitta, L. C. P. M. de Smet, *Adv. Funct. Mater.* **2021**, *31*, 2105203.
[54] S. Kim, H. Yoon, D. Shin, J. Lee, J. Yoon, *J. Colloid Interface Sci.* **2017**, *506*, 644.
[55] T. Setayeshmanesh, M. M. Parivazh, M. Abbasi, S. Osfouri, M. J. Dianat, M. Akrami, *Sustainability* **2022**, *14*, 2298.